

Geometric Prior Based Deep Human Point Cloud Geometry Compression

Xinju Wu, Pingping Zhang, Meng Wang, *Member, IEEE*, Peilin Chen, Shiqi Wang, *Senior Member, IEEE*, and Sam Kwong, *Fellow, IEEE*

Abstract—The emergence of digital avatars has raised an exponential increase in the demand for human point clouds with realistic and intricate details. The compression of such data becomes challenging with overwhelming data amounts comprising millions of points. Herein, we leverage the human geometric prior in geometry redundancy removal of point clouds, greatly promoting the compression performance. More specifically, the prior provides topological constraints as geometry initialization, allowing adaptive adjustments with a compact parameter set that could be represented with only a few bits. Therefore, we can envisage high-resolution human point clouds as a combination of geometric priors and structural deviations. The priors could first be derived with an aligned point cloud, and subsequently the difference of features is compressed into a compact latent code. The proposed framework can operate in a play-and-plug fashion with existing learning based point cloud compression methods. Extensive experimental results show that our approach significantly improves the compression performance without deteriorating the quality, demonstrating its promise in a variety of applications.

Index Terms—Point cloud compression, neural network, geometric prior

I. INTRODUCTION

RECENT years have witnessed unprecedented growth in the demand and development of Extended Reality (XR) and Metaverse, which brings enormous benefits to applications such as virtual social, online education, e-commerce, tourism, and exhibition. Metaverse provides us with a collective virtual shared space where users can incarnate into digital avatars to communicate and interact with others. In parallel, three-dimensional (3D) acquisition devices like RGBD cameras, 3D scanners, and LiDAR have become increasingly precise and cost-effective, which caters to the need to handily create the digital twin that has a realistic shape and appearance with the physical human. While meshes have traditionally been used to create virtual human models, they can be expensive and time-consuming to generate, particularly for detailed and lifelike models. An efficient and versatile alternative to represent humans is point clouds, allowing for more accessible and accurate 3D scanning and modeling of human bodies and faces with intricate details.

A point cloud is a collection of 3D data points that embody the surface geometry of an entity, typically captured through hardware devices such as LiDAR or photogrammetry

Xinju Wu, Pingping Zhang, Meng Wang, Peilin Chen, Shiqi Wang, and Sam Kwong are with the Department of Computer Science, City University of Hong Kong, Hong Kong, China, (e-mail: xinjuwu2-c@my.cityu.edu.hk; ppingyes@gmail.com; mwang98-c@my.cityu.edu.hk; plichen3-c@my.cityu.edu.hk; shiqiwang@cityu.edu.hk; cssamk@cityu.edu.hk).

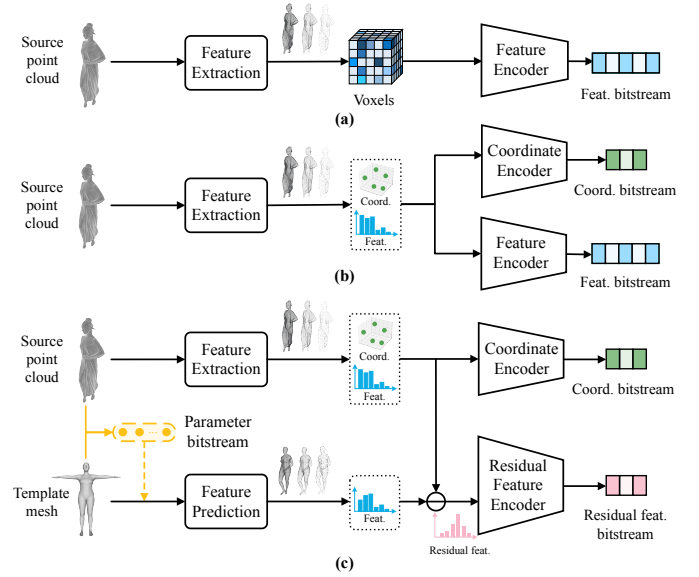


Fig. 1. Comparisons of human point cloud geometry compression paradigms. The existing approaches directly preserve informative geometric features by the feature extraction module, such as (a) compressing features based on 3D voxels or (b) compressing coordinates and features individually. (c) The proposed scheme incorporates geometric priors to remove the redundancy at the feature level, followed by residual feature compression, yielding better compression performance.

by RGBD cameras. Each point encompasses a coordinate in 3D space, with additional information such as color, normal, intensity, and reflectivity. To satisfy the requirements of high fidelity with a high level of detail, point clouds generally contain an astronomical amount of spatial data, numbering in the millions, or even billions. For instance, a high-resolution point cloud of a full-body human from 8i’s dataset [1] contains 765,000 3D points, each comprising a 30-bit coordinate (x, y, z) and 24-bit color information (r, g, b) in total, resulting in a storage size of 11 MBytes for a point cloud. If we consider a dynamic human point cloud sequence of 300 frames, it would occupy a storage space of approximately 3 GBytes to display a 10-second volumetric video. The overwhelming data volume poses incredible challenges to the processing, transmission, and storage of high-quality point clouds. It is imperative to research Point Cloud Compression (PCC) under the cost restraints.

The traditional PCC methods developed by the Moving Picture Experts Group (MPEG) [2], [3] can be categorized into Video-based PCC (V-PCC) [4] for dynamic point clouds

and Geometry-based PCC (G-PCC) [5] for static point clouds. V-PCC [4] projects point clouds into two-dimensional (2D) planes and utilizes the hybrid video coding standard (e.g., High Efficiency Video Coding) for compression. G-PCC [5] utilizes octree coding, trisoup coding, and predictive coding for geometry compression, while region adaptive hierarchical transform and lifting transform are leveraged for attribute compression. On the other hand, deep learning based techniques have been successfully applied to PCC, leveraging the end-to-end training methodology [6], [7]. These approaches typically rely on the autoencoder architecture, consisting of an encoder of stacked downscaling blocks to compress the source point clouds into a compact latent code, and a decoder of upscaling blocks to reconstruct the original point sets from the latent code. The neural networks are trained towards the optimization of the rate-distortion (RD) performance. These techniques have shown promising improvements for point cloud geometry and attribute compression by enabling the identification and prioritization of critical features.

Despite the demonstrated success in learning-based PCC [8]–[10], existing works typically ignore the prior knowledge of the object, as shown in Fig. 1(a) and 1(b). However, human bodies possess regular structures that can be effectively leveraged as explicit prior knowledge in compressing high-resolution human point clouds. Inspired by this, we propose a novel deep human point cloud geometry compression framework based on an explicit geometric prior, providing hard topological restrictions as an initialization of geometry, as illustrated in Fig. 1(c). Our framework utilizes a set of parameters with only a few bits to drive a geometric prior model, enhancing point cloud geometry compression. Our main contributions are summarized as follows:

- We propose a novel geometric prior based point cloud geometry compression framework where human point clouds can be compressed as the combination of geometric priors and structure variations. Based on the prior at the feature level, the redundancy is greatly removed to improve the coding performance.
- We explore the 3D parametric model for PCC that endows topological constraints as an initialization for effective deep feature coding. This hybrid approach combines the strengths of both mesh and point cloud representations, such that the representation with fewer bits while flexible in representing complex shapes and fine-grained details can be achieved.
- We incorporate our methodology as a plug-and-play manner in the point cloud geometry compression. It is manifested that our approach yields superior RD performance compared to different baselines, exhibiting the superiority of the proposed scheme.

II. RELATED WORKS

A. Traditional Point Cloud Geometry Compression

The division of the point cloud based on an octree has been widely adopted in conventional approaches for compressing point cloud geometry, where only non-empty nodes among eight children continue to be subdivided. Mekuria *et*

al. [11] first proposed a hybrid time-varying point cloud codec that serves as the anchor for MPEG PCC [2], [3]. In this codec, each intra-frame is progressively coded in the octree subdivision using 8-bit occupancy codes, while inter-frame redundancy is eliminated using the rigid transformation of 3D macroblocks in the octree voxel space. The MPEG has also developed the prevailing G-PCC and V-PCC standards [2], [3]. G-PCC [4] relies on three techniques for geometry compression, including octree coding, trisoup coding, and predictive coding. Octree coding employs several modes to predict compact occupancy codes for isolated nodes, planes, and patterned regions, followed by an arithmetic coding engine. Trisoup coding aims to achieve lossy compression by using a pruned octree for surface reconstruction and resampling. Predictive coding targets at large-scale LiDAR point clouds in low latency cases by pointwise prediction in tree-based traversal. By contrast, V-PCC [5] adopts another line of compression by projecting 3D patches of point clouds onto the surfaces of a bounding box using a 3D-to-2D projection, thus allowing for the reuse of existing video codecs [12]. The projection result of the geometry component is a 2D depth map where each value represents the distance between each point and the projection plane.

Various techniques have been proposed to improve the geometry coding performance of both G-PCC and V-PCC. Specifically, for G-PCC [4], Silhouette decomposition [13], Dyadic decomposition [14], quad-tree and binary-tree partitions [15], and triangle construction [16] are used to enhance octree coding and trisoup coding. For V-PCC [5], block partitioning [17], frame padding [18], and motion prediction [19] are employed, along with the optimization on geometric error projection based rate-distortion optimization (RDO) [20]. Additionally, coding approaches detached from MPEG PCC [2], [3] have also been explored. For instance, Oliveira *et al.* [21] employed a graph-based transform for the enhancement layer and an octree-based approach for the base layer. Furthermore, Zhu *et al.* exploited region similarity [22] and view-dependent projection [23], while Krivokuća *et al.* [24] introduced volumetric functions for geometry compression. In inter-frame compression, various methods for 3D motion compensation [25], [26] and context-based arithmetic coding [27] have also been investigated.

B. Learning-based Point Cloud Geometry Compression

Recently, there has been a surge of interest in learning-based point cloud geometry compression. One direction involves the development of an efficient entropy model that leverages context, primarily for large-scale point clouds. Huang *et al.* [28] proposed a conditional entropy model with multiple ancestor nodes in the octree representation, whereas Que *et al.* [29] developed VoxelContext-Net, which utilizes information from neighboring octree nodes at the same depth level to improve local voxel context. Moreover, Fu *et al.* [30] utilized sibling nodes to expand context and an attention mechanism to emphasize key nodes, while children of sibling nodes and surface prior are further investigated in [31]. For dynamic cases, Biswas *et al.* [32] proposed an entropy model that models

the probabilities of octree symbols and intensity values by exploiting spatial and temporal redundancy between successive LiDAR point clouds.

Another direction for learning-based point cloud geometry compression involves downsampling points in the encoder and recovering them in the decoder, extending end-to-end image [6], [7] or video [33], [34] compression techniques. Researchers have explored several techniques in learning-based PCC, such as voxelization followed by 3D convolution, sparse convolution, and Multi-Layer Perceptron (MLP). For example, Quach *et al.* [8], [35] and Nguyen *et al.* [36], [37] converted point clouds into 3D grids using voxelization and represented each voxel with an occupied or unoccupied state. Guarda *et al.* explored learning-based scalable coding for geometry [38], [39] and obtained multiple rate-distortion points from a trained model using explicit quantization of the latent representation [40]. Milani [41] introduced an adversarial autoencoding strategy to train the encoder. Wang *et al.* [42] proposed the PCGC framework, which includes pre-processing, autoencoder, and post-processing modules, and uses Voxception-ResNet (VRN) [43] within the stacked unit and a hyperprior entropy model. As the representative of sparse convolution based methods, a multiscale framework, PCGCv2, was proposed by Wang *et al.* [9] based on sparse tensors to avoid processing of massive empty voxels. To further improve the efficiency, they developed a more elaborate structure with downscaling and upscaling in each scale to calculate occupancy probability [10], and this technique has been applied in LiDAR point clouds through neighborhood point attention [44]. PointNet-based methods [45]–[48] for point cloud compression employ set abstraction layers to extract local features, drawing inspiration from classification and segmentation tasks. More specifically, self-attention layers in Transformer have been first introduced by Liang *et al.* [45]. Furthermore, density, local position, and ancestor embeddings can be utilized to preserve local density information [46]. Regarding inter-frame compression, Akhtar *et al.* [49] utilized sparse convolution to map the latent code of the previous frame to the coordinates of the current frame. Meanwhile, Fan *et al.* [50] proposed a multiscale motion flow fusion module for motion estimation and developed an adaptive weighted interpolation algorithm to further enhance motion estimation accuracy.

However, current learning-based point cloud geometry compression techniques commonly ignore the prior knowledge of the source 3D model, resulting in geometric redundancy during the compression process. Incorporating prior knowledge into the source 3D model, such as its geometric properties, topology, or semantic information, will undoubtedly improve the coding efficiency.

C. Representations from 3D priors

Substantial attempts have also been made to retain explicit 3D geometric priors for 2D processing. Yang *et al.* [51] manipulated a 3D morphable model as the face prior to transform a face between image space and UV texture space, which benefits image inpainting. Additionally, researchers have explored the enhancement of single-view images in the wild by

concatenating regressed 3D shapes from 2D facial images and decoded results from face embedding [52], or decomposing human and object images into 3D representations such as depth, normals, and albedo [53], [54]. In compression research, Chen *et al.* [55] recently proposed an interactive face video coding framework that converts inter frames into 3D meshes and re-projects them in the decoder, demonstrating promising performance in ultra-low bitrate face communications.

For 3D processing, various methods have been developed to leverage 3D geometric prior information. Self-prior [56], [57] is utilized to model repeating geometric structures and leverage self-correlation across multiple scales with fine-grained details. In [58], a parameterized 3D representation of Coons patches is used to represent a 3D object, which is optimized iteratively based on a deformable parameterized template model with a minimal number of control points. For human data, the Skinned Multi-Person Linear model (SMPL) [59] is an expressive 3D full-body template model that can be utilized as a 3D prior. In [60], the predicted parameters from the SMPL model are fed to a recognition module for improved pose estimation. Despite the increasing use of 3D priors in various applications, few attempts have been made in incorporating 3D priors in point cloud compression.

III. METHODOLOGY

A. Overview

In this work, we propose a learning-based human point cloud geometry compression approach, which leverages the human geometric priors to improve the compression performance. The general architecture of the proposed scheme is shown in Fig. 2. Specifically, the first stage in the encoding process is to obtain the geometric prior representation, which begins with fitting the high-resolution source point cloud from a predefined template to derive succinct parameters. As the body modeling strategy and the mesh template are available during encoding and decoding, only the parameter set needs to be encoded and conveyed by the corresponding bitstream. Although the general template mesh can be aligned globally based on these parameters and sampled to create a similar-shaped point cloud with the input, differences still exist in the detailed point positions. To address this issue, we adopt deep learning modules to extract high-level embeddings for both the source and aligned point clouds and conduct the warping operations in the feature domain. This enables the aligned point cloud with enhanced representation capability, leading to more compact residual features with fewer data amounts to be transmitted in the bitstream. In particular, the coordinates of a downsampled input point cloud are losslessly encoded, and their point features are subtracted by the point features generated by the aligned point clouds. These residual features are further compressed using a well-designed entropy model. It is worth mentioning that we adopt the same modules with the same weights for mesh-to-point-cloud conversion, feature extraction, and feature warping in the decoding process to maintain consistency on both sides, ensuring the faithful reconstruction of the high-quality point cloud.

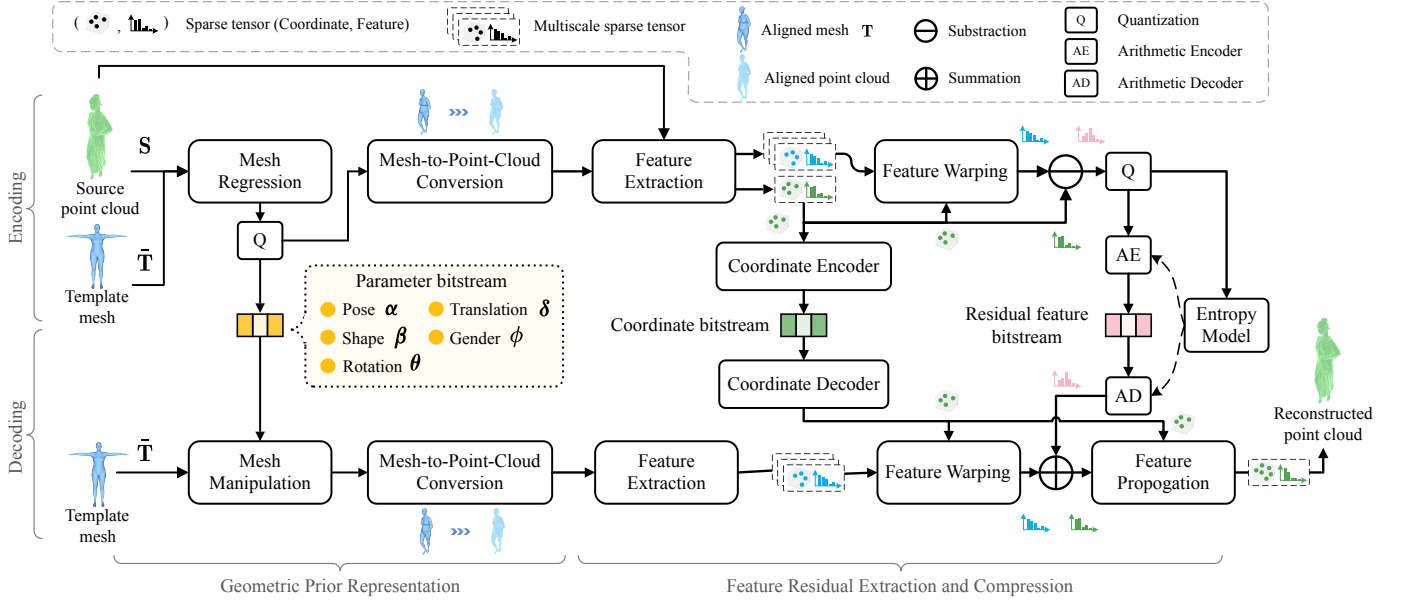


Fig. 2. Overview of our proposed framework that involves a two-stage process for geometric prior representation and feature residual compression. Given a source point cloud S , we first regress an aligned mesh T that can be driven by a set of parameters from a deformable template mesh \bar{T} . During encoding, these parameters are further quantized into a compact bitstream, allowing for the manipulation of the template mesh’s pose and shape during decoding. Regarding the next stage, we extract features from both the source point cloud and an aligned point cloud based on the sparse tensors that comprise of coordinates and features. We then warp the features of the aligned point cloud onto the coordinates of the source point cloud, subsequently calculating feature residuals. These residuals are further encoded with guidance from an entropy model. The decoder, situated at the lower part of the framework, processes bitstreams to initiate the decoding process.

B. Geometric Prior Representation

We utilize the SMPL model [59] as our geometric prior to construct a comparable human point cloud, which can accurately derive a diverse range of body shapes and poses in a compact, flexible, and expressive manner. The mean template used in our work can be manipulated by a collection of parameters,

$$\Sigma = \{\alpha, \beta, \theta, \delta, \phi\}, \quad (1)$$

where $\alpha \in \mathbb{R}^{69}$, $\beta \in \mathbb{R}^{10}$, $\theta \in \mathbb{R}^3$, $\delta \in \mathbb{R}^3$, $\phi \in \mathbb{R}$ represent pose, shape, rotation, translation, and gender, respectively. The shape parameter determines regional variations while the pose parameter controls joint rotations in the body.

The mesh manipulation module combines geometric variation and surface deformation to model the human body, which enables extensively customizable and realistic representations. With the predicted parameters, it is possible to represent vertex deviations from the template as

$$\mathbf{V} = \bar{\mathbf{T}} + B_{\text{shape}}(\beta) + B_{\text{pose}}(\alpha), \quad (2)$$

where $\bar{\mathbf{T}}$ denotes the mean template model. The functions B_{shape} and B_{pose} account for the effects of shape and pose dependent deformations. Based on proximity to the skeleton, surface deformation assigns weights to each vertex of the model,

$$\mathbf{T} = H(\beta, \theta)\mathbf{V} + \delta, \quad (3)$$

where the function H first determines the joint positions influenced by the shape and then expresses the global rotation transformation of these joints.

To regress a human point cloud with a parametric human model, we utilize the technique introduced by Zuo *et al.* [54],

which involves utilizing a pretrained PointNet++ [61] network in conjunction with a probabilistic correspondence association module. The resulting predicted parameters are quantized and encoded into a bitstream. To ensure the encoder and the decoder to be fully synchronized, we recover an aligned mesh from the quantized parameters in the mesh manipulation block. This reconstructed mesh is then fed into mesh-to-point-cloud conversion via the Poisson-disk sampling algorithm [62], generating an aligned point cloud with the similar shape.

C. Feature Residual Extraction and Compression

Using the analogous point cloud predicted from the geometric prior, geometry compression performance of the source point cloud can be promoted by redundancy removal. Specifically, we extract high-level feature representations of the source and the aligned point clouds separately using stacked downsampling blocks. Since the aligned point cloud refers to a coarse approximation of the target positions, we carry out warping operations within the feature space, following the techniques used in deep video compression for feature-level motion estimation and motion compensation [33]. More precisely, we warp the features of the aligned point cloud onto the coordinates of the source point cloud using sparse convolution. This allows us to obtain compact residual features through feature subtraction, followed by the compression of residual features. It is worth noting that our proposed pipeline is versatile and can be applied in a plug-and-play fashion by swapping out the feature extraction and warping modules with a variety of approaches. In our implementation, we inherit the feature extraction and warping techniques from the

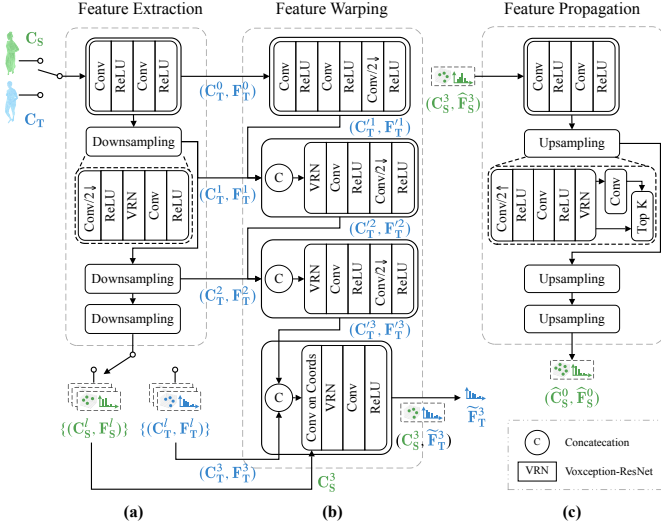


Fig. 3. The network structure of (a) feature extraction, (b) feature warping, and (c) feature propagation modules. The input of the feature extraction module can be coordinates of the source point cloud C_S or the aligned point cloud C_T . “Conv/2↓” and “Conv/2↑” represent the convolution and transposed convolution operations with the stride of 2. “Conv on Coords” convolves on target coordinates using a generalized transposed sparse convolution layer. We consider an example with three scales, where $L = 3$.

forementioned deep point cloud compression approaches [9], [42], [49] based on sparse convolution [63] to retain essential and critical point characteristics.

In sparse convolution techniques, intermediate outcomes between modules are represented by sparse tensors. Specifically, a sparse tensor \mathcal{X} saves only non-zero elements using a coordinate-feature pair $\mathcal{X} \Leftrightarrow (C, F)$. Each non-zero coordinate $(x_i, y_i, z_i) \in C$ corresponds to the associated feature $f_i \in F$, enabling accurate representation with abundant contexts. By applying convolutional filters only to non-zero elements, sparse convolution significantly reduces computational complexity and memory usage. Sparse convolution [63], [64] specified in the 3D space is referred to as

$$f_u^{\text{out}} = \sum_{i \in \mathcal{N}^3(\mathbf{u}, C^{\text{in}})} W_i f_{\mathbf{u}+i}^{\text{in}} \text{ for } \mathbf{u} \in C^{\text{out}}, \quad (4)$$

where input and output coordinates C^{in} and C^{out} correspond to input and output feature vectors F^{in} and F^{out} , respectively. The set \mathcal{N}^3 denotes a 3D kernel with an arbitrary shape, and its subset $\mathcal{N}^3(\mathbf{u}, C^{\text{in}}) = \{\mathbf{i} | \mathbf{u} + \mathbf{i} \in C^{\text{in}}, \mathbf{i} \in \mathcal{N}^3\}$ contains the offsets from the current 3D coordinate \mathbf{u} that exist in C^{in} . The kernel weight is denoted by W . In our implementation, the kernel is defined as a hypercube with a size of 3, namely $[-1, 0, 1]^3$, and the Minkowski [64], [65] is adopted as the sparse inference engine.

1) *Feature Extraction*: Using sparse convolution as the essential operation, the feature extraction module is carefully designed to enable high-level embedding prediction. Following learning-based compression methods [9], [10], the proposed approach works in a bottom-up manner by progressively reducing the spatial resolution and exponentially increasing the receptive field. As shown in Fig. 3(a), each downsampling block in the feature extractor comprises a strided convolution,

a VRN unit [42], [43], and another convolution layer in a cascading manner. Specifically, the strided convolution reduces the number of points, while the subsequent convolution layer refines extracted features for optimal performance. The VRN [43] unit, located between the two convolution layers, utilizes skip connections to mitigate information loss during training and employs parallel convolutional layers with varying kernel sizes, namely $1 \times 1 \times 1$ or $3 \times 3 \times 3$, to capture features at different ranges. By stacking these downsampling blocks, the feature extraction module outputs multiscale sparse tensors, including coordinates and features, that form the latent representation of an entire point cloud. As such, the extracted features can reconstruct the original geometry information in a hierarchical manner with only a small number of output coordinates as indispensable information to decrease required bits. We losslessly encode these coordinates using a coordinate encoder [5], and further process multiscale features in the following modules.

2) *Feature Warping*: The feature warping module is designed to transform the extracted features from the aligned point cloud to the coordinates of the source point cloud. This process is completed in a coarse-to-fine manner, with each scale entailing a hierarchical concatenation of primary sparse tensors \mathcal{X} from the feature extractor and auxiliary sparse tensors \mathcal{X}' from the previous block, as illustrated in Fig. 3(b). To this end, the preceding block utilizes a strided convolution layer similar to the feature extraction module. By performing this concatenation, we can enrich some informative points upon the downscaled output of the feature extraction module for subsequent blocks.

In the final block of the module, the concatenated features of the aligned point cloud are convolved on downscaled coordinates of the source point cloud using a generalized sparse transposed convolution layer [49], [63]. The process can be represented succinctly as

$$(C_S^L, \tilde{F}_T^L) = G(\mathcal{X}_T^L \oplus \mathcal{X}'_T^L, C_S^L), \quad (5)$$

where \oplus denotes the concatenation operation of the down-scaled primary \mathcal{X}_T^L and auxiliary sparse tensors \mathcal{X}'_T^L , and the function G represents the operations predominantly performed by the layer that convolves on target coordinates [65], which is illustrated in Fig. 4(a). As shown in this figure, each 3D point is represented by a 2D grid where the grid position indicates the point’s 3D coordinate and the grid color represents its feature. As can be observed, during the operation of convolution on coordinates, the output point D retains the same coordinate as the target point C, while its feature is determined by input points A and B within the receptive field. After the operation of convolution on coordinates, the output sparse tensor comprises coordinates of the source point cloud C_S^L and warped features of the aligned point cloud \tilde{F}_T^L from the last scale L . This allows our approach to fix the output coordinates and capture essential information from the input.

3) *Residual Feature Calculation*: After obtaining warped features of the aligned point cloud, it is straightforward to perform feature-level subtraction. Recent works on dynamic PCC [49], [50] have performed inter prediction in the feature

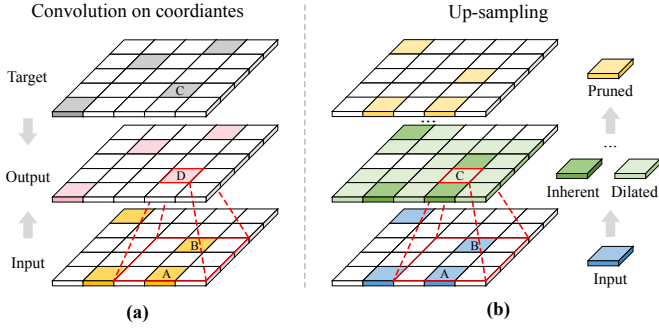


Fig. 4. The 2D illustration of essential components in feature warping and feature propagation modules. (a) The convolution on coordinates layer in feature warping; (b) an upsampling block in feature propagation.

space. Following this vein, the proposed framework aims to factor out redundancy between a source point cloud and its variant in the feature domain. Specifically, we subtract the warped features of the aligned point cloud $\tilde{\mathbf{F}}_T^L$ from the features of the source point cloud \mathbf{F}_S^L , resulting in residual features. This process can be formulated as

$$\Delta \mathbf{F}^L = \mathbf{F}_S^L - \tilde{\mathbf{F}}_T^L, \quad (6)$$

where $\Delta \mathbf{F}^L$ denotes feature residuals in the last scale L . Feature-level alignment avoids the challenge of directly computing offsets in Euclidean space, which can be difficult due to the inherent complexity of accurately matching unordered points. Analogously, this attempt has also been proven to be effective in deep video compression [33]. It shrinks prediction errors caused by optical flow-based motion compensation in the pixel domain by computing feature-level residuals between extracted features and motion-warped features.

4) *Residual Feature Compression*: To compress residual features, we add a uniform quantizer to the latent code, thereby implementing vector quantization on original signal space. Subsequently, we estimate the entropy of the residual features and apply arithmetic encoding for further compression. Specifically, the incorporation of additive uniform noise for features during the training phase allows for the approximation of the rounding operation and ensures differentiability within the optimization process. During the inference phase, rounding is directly applied. After quantization, the entropy of the latent representation is estimated using an entropy bottleneck based a non-parametric factorized model [6] that constructs an independent probability density model for each channel. The selected entropy model can be further extended to advanced approaches with a hyperprior [7] or joint autoregressive hierarchical priors [66].

D. Decoding

The total bitstream is comprised of three components, including parameters, coordinates, and residual features. The parameters are utilized to generate a variant point cloud, from which features are extracted and residual features are added to reconstruct the original geometry of the input. Specifically, the parameters are first decoded to manipulate the template mesh, which is accessible in both the encoding and decoding

processes as shown in Fig. 2. Subsequently, a reconstructed aligned mesh serves as the input for the mesh-to-point-cloud conversion, producing an aligned point cloud. This is followed by a feature extraction module that captures multiscale high-level embeddings. These predicted features of the aligned point cloud are warped onto a decoded set of coordinates corresponding to skeleton points of a source point cloud. Meanwhile, residual features are decoded from the bitstream and added to the previously obtained warped features, resulting in the recovered features of the source point cloud. These features are subsequently propagated to upscale the points close to the source point cloud.

The feature propagation module mainly employs a transposed convolution layer with a two-stride in each upsampling block, as depicted in Fig. 3(c), to upscale the input coordinate set while retaining its sparsity pattern. The outcome of transposed convolution is demonstrated in the intermediate layer shown in Fig. 4(b), where light green grids represent dilated points absent in the input and dark green grids correspond to inherent coordinates of the input. The transposed convolution layer may generate overlapping regions, as portrayed by point C belonging to both the generated regions of points A and B. To remove dispensable points and sustain information fidelity, an additional convolution layer and a pruning layer are attached after the VRN [43] in each upsampling block. The convolution layer determines the probability of a point being occupied, while the pruning layer eliminates points with low occupancy probability and preserves only the top K points. Here, K corresponds to the number of points in the input. Furthermore, hierarchical skip connections are introduced during training to allow upsampled points to retrieve fine-grained details of the source point cloud with the aid of multiscale features from the feature extractor.

E. Loss Function

The objective of point cloud geometry compression is to minimize the number of required bits while maintaining maximum reconstruction quality of geometry. To this end, we optimize the RD tradeoff loss function,

$$\mathcal{L} = \lambda R + D, \quad (7)$$

where the Lagrange multiplier λ balances rate R and distortion D . Only the rate of feature residuals is represented by R , as the compression of both manipulation parameters and downsampled coordinates is excluded from the optimization process. To bypass the difficulty of matching unordered points, we employ probability-based methods to calculate coordinate errors. The distortion is determined by the sum of the binary cross entropy (BCE) [65] in each scale,

$$\begin{aligned} D &= \sum_{l=1}^L \text{BCE}^l(\mathcal{X}_S^l, \hat{\mathcal{X}}_S^l) \\ &= \sum_{l=1}^L \frac{1}{N^l} \sum_{i=1}^{N^l} -x_i \log(p_i) - (1-x_i) \log(1-p_i), \end{aligned} \quad (8)$$

where \mathcal{X}_S^l and $\hat{\mathcal{X}}_S^l$ denotes the source and decoded sparse tensors in scale $l = 1, \dots, L$ with $L = 3$ in our implementation,

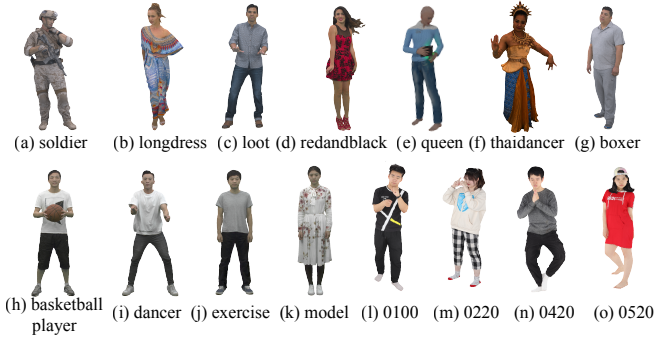


Fig. 5. The training and testing datasets. Multiple frames of sequences from (a) *soldier* to (e) *queen* are utilized for training. A single frame of sequences from (f) *thaidancer* to (o) 0520 is employed for testing.

and N^l represents the number of decoded points in scale l . A binary occupancy value x_i indicates the inclusion or exclusion of a decoded point i as part of the source, and p_i denotes the probability of that point being occupied.

IV. EXPERIMENTS

A. Implementation Details

1) *Datasets*: We conduct a series of experiments on prevailing high-resolution human point cloud datasets, namely 8i Voxelized Full Bodies (8iVFBv2) [1], OwlII dynamic human dataset (OwlII) [67], THuman2.0 [68], and 8i Voxelized Surface Light Field (8iVSLF) [69], as shown in Fig. 5 and summarized in Table I. The 8iVFBv2 dataset [1] and the sequence *queen* from MPEG PCC [70], [71] are used for training. The former contains four sequences with 300 frames each, while the latter includes 250 frames. Due to GPU memory limitations, each point cloud is partitioned into four patches using a KD-tree, thus resulting in a total of 5800 3D patches for training. During testing, we employ the entire human point clouds for inference, using point clouds from standardization committees: *basketball player*, *dancer*, *exercise*, *model* sequences from OwlII [67], *thaidancer* and *boxer* from 8iVSLF [69]. To further demonstrate the generalization capability, we also utilize high-quality human scans from the publicly available and challenging THuman2.0 dataset [68], which are processed into point clouds with the midpoint subdivision algorithm and employed as testing data. Furthermore, the geometry precision for point clouds, as indicated in the last column of Table I, represents the number of distinct values along each axis of the 3D coordinates. For instance, with a geometry precision of 10 bits, the x , y , and z values for each point range from 0 to 1023.

2) *Performance evaluation*: The quantitative evaluation assesses the performance of our approach based on the RD criteria by computing Bjøntegaard delta rate (BD-Rate) and Bjøntegaard delta peak signal-to-noise ratio (BD-PSNR) results. The bitrate is calculated by total bitstreams of prior parameters, downscaled coordinates, and feature residuals, and the measurement is reported as bits per point (bpp). The geometric distortion is calculated by point-to-point (D1) and point-to-plane (D2) errors [70], [71]. D1 computes the distance by connecting each point in a distorted point cloud and its

TABLE I
THE DETAIL OF POINT CLOUDS USED IN TRAINING AND TESTING.

Dataset	Point cloud	# points	# frames	Precision
8iVFBv2 [1]	soldier	1,059,810	300	10
	longdress	765,821	300	10
	loot	784,142	300	10
	redandblack	729,133	300	10
8iVSLF [69]	queen	1,006,509	250	10
	thaidancer	979,857	1	10
	box	994,546	1	10
OwlII [67]	basketball player	2,880,057	1	11
	dancer	2,592,758	1	11
	exercise	2,391,718	1	11
	model	2,458,429	1	11
THuman2.0 [68]	0100	2,391,718	1	10
	0200	847,940	1	10
	0420	766,152	1	10
	0520	770,210	1	10

closest points in the reference point cloud, and D2 derives a new distance vector by projecting the original distance vector along the normal direction. Following the MPEG common test conditions (CTC) [70], [71], we calculate the peak signal-to-noise ratio (PSNR) value over the symmetric D1 and D2. More specifically, we first apply the source point cloud as a reference to evaluate the decoded point cloud. Then, we swap them and compute the maximum PSNR value between these two paradigms to obtain the symmetric distortion.

3) *Training procedure*: The training procedure focuses on the coding of residual features produced by subtracting features of the source and aligned point clouds. We train seven models using different factors λ in Eqn. (7), specifically $\lambda \in \{0.2, 0.5, 1.1, 2.5, 6, 9, 13\}$. Our methodology is accomplished on a machine with a NVIDIA GeForce RTX 3090 GPU in memory of 24GB, and we implement three scales in the hierarchical structure. We set the batch size as 8 and train the model for 64 epochs. The Adam optimizer is employed with weight decaying and the initial value is set to $16e - 4$. It is worth mentioning that the compression of predicted geometric prior parameters and downsampled coordinates is not included in the training procedure. We obtain predicted parameters by using the pretrained model from [54] in our mesh regression module, and these parameters are rounded to three decimal places. For downsampled coordinates, we encode them losslessly using G-PCC [4].

B. Performance Comparisons

Herein, we report the point cloud geometry coding performance and compare our proposed framework to other approaches to showcase the superiority of our methodology.

1) *Baselines*: To validate the effectiveness of our framework, we conduct a comparative study of various point cloud geometry compression techniques, including traditional and learning-based approaches. G-PCC [4] and V-PCC [5] are representative techniques for conventional codecs, and PCGC [42] and PCGCv2 [9] are learning based baselines. Specifically, G-PCC and V-PCC are examined using the latest version available, i.e., TMC13v14 for G-PCC and TMC2v18

TABLE II
BD-RATE AND BD-PSNR RESULTS AGAINST THE BASELINES G-PCC (OCTREE) [4], G-PCC (TRISOUP) [4], V-PCC [5], PCGC [42], PCGCv2 [9] ON DATASETS OWLII [67], 8iVSLF [69], AND THUMAN2.0 [68] USING D1 AND D2 ERRORS [70], [71]

Dataset	Sequence	BD-Rate with D1 PSNR (%)					BD-PSNR with D1 (dB)				
		G-PCC (octree)	G-PCC (trisoup)	V-PCC	PCGC	PCGCv2	G-PCC (octree)	G-PCC (trisoup)	V-PCC	PCGC	PCGCv2
8iVSLF	boxer	-93.92	-93.62	-50.02	-67.96	-32.60	12.77	7.89	2.65	5.16	1.48
	thaidancer	-91.85	-87.86	-48.48	-61.25	-22.42	11.56	7.81	2.65	4.83	1.04
Owlii	basketball player	-95.42	-98.36	-93.54	-69.61	-29.31	13.60	9.03	8.47	5.08	1.19
	dancer	-95.20	-97.75	-94.03	-68.98	-30.30	13.51	9.19	8.82	4.95	1.23
	exercise	-95.07	-98.22	-93.12	-68.19	-30.84	13.55	8.81	8.54	4.89	1.29
	model	-93.94	-94.10	-91.24	-75.77	-32.73	12.86	8.70	8.62	6.58	1.54
THuman2.0	0100	-89.54	-75.01	-19.08	-64.87	-26.80	9.13	5.02	0.55	4.03	1.10
	0220	-88.64	-75.72	-37.71	-57.37	-20.60	9.04	5.15	1.38	3.47	0.91
	0420	-90.20	-77.84	-30.34	-56.38	-33.06	9.62	5.22	1.04	3.17	1.37
	0520	-89.60	-74.59	-36.18	-59.39	-28.35	9.29	5.06	1.29	3.40	1.29
Average with D1		-92.34	-87.31	-59.37	-64.98	-28.70	11.49	7.19	4.40	4.56	1.25
Dataset	Sequence	BD-Rate with D2 PSNR (%)					BD-PSNR with D2 (dB)				
		G-PCC (octree)	G-PCC (trisoup)	V-PCC	PCGC	PCGCv2	G-PCC (octree)	G-PCC (trisoup)	V-PCC	PCGC	PCGCv2
8iVSLF	boxer	-90.90	-92.23	-49.28	-64.72	-30.16	12.08	8.99	3.01	5.00	1.59
	thaidancer	-88.36	-88.38	-51.75	-61.64	-22.50	10.87	8.43	3.20	4.76	1.17
Owlii	basketball player	-92.38	-96.73	-86.81	-70.48	-25.70	12.46	9.18	8.64	5.79	1.27
	dancer	-92.18	-95.61	-87.66	-70.25	-26.06	12.35	9.23	8.96	5.37	1.27
	exercise	-91.88	-96.02	-86.48	-68.13	-26.79	12.36	9.30	8.71	5.42	1.35
	model	-89.79	-90.97	-85.89	-68.29	-27.97	11.27	9.02	8.85	6.11	1.50
THuman2.0	0100	-86.58	-80.36	-37.43	-72.03	-21.94	9.32	6.38	1.60	2.65	0.98
	0220	-86.56	-83.43	-56.99	-58.65	-13.93	9.47	7.16	3.23	3.24	0.64
	0420	-87.73	-82.52	-45.90	-66.95	-15.72	9.96	7.08	2.27	2.60	0.74
	0520	-88.16	-84.53	-55.13	-71.29	-15.21	9.85	7.21	2.89	2.56	0.68
Average with D2		-89.45	-89.08	-64.33	-67.24	-22.60	11.00	8.20	5.13	4.35	1.12

in All-Intra mode for V-PCC. We compare two branches of G-PCC for geometry compression, namely, the octree-based and surface reconstruction based (trisoup) schemes. Our quantization parameter settings for G-PCC (octree), G-PCC (trisoup), and V-PCC follow CTC [70], [71], with the bitstream compositions for attribute disregarded. For learning-based baselines, PCGC employs point cloud voxelization and stacked 3D convolutions to capture compact features, while PCGCv2 leverages sparse convolution layers in a multiscale manner. It is worth mentioning that our framework is versatile and compatible with a play-and-plug setup, and the feature extraction component shown in our framework utilizes the same network structure as PCGCv2. For fair comparisons, a factorized prior model [6] is employed as the entropy model in learning-based baselines and our approach.

2) *Experimental results:* In Table II, we report the BD-Rate and BD-PSNR results of the proposed framework against G-PCC (octree), G-PCC (trisoup), V-PCC, PCGC, and PCGCv2 with D1 and D2 errors as distortion and bpp as bitrate. It is observed that our approach achieves significant bitrate savings and BD-PSNR gains compared to these traditional and learning-based methods on human point clouds from various datasets. Specifically, our method outperforms G-PCC (octree) with an average of 92.34% and 89.45% bitrate savings in terms of D1 and D2, respectively. Significant improvement has also been noticed against G-PCC (trisoup) and V-PCC with more than 87% and 59% BD-Rate gains individually regarding both distortion errors. When compared with learning-based methods such as PCGC and PCGCv2, we achieve 64.98% and 28.70% bitrate savings in terms of D1, respectively. In particular, our approach has around 1.26 dB gains over PCGCv2 on

the 8iVSLF dataset, 1.31 dB on Owlii, and 1.17 dB on THuman2.0. As PCGCv2 shares the same feature extraction network structure as ours, the performance improvement is a clear indication of the effectiveness of incorporating geometric priors and residual features. Our approach also outperforms learning-based baselines with respect to D2 errors.

As shown in Fig. 6, our proposed framework yields superior RD performance compared with other traditional and learning-based methods on diverse human point clouds in terms of D1 PSNR. It is not surprising to observe that our method achieves more gains at 0.15 bpp than 0.05 bpp when compared with PCGCv2. This can be attributed to the fact that the coordinates of downsampled points must be encoded losslessly and residual features take up a larger proportion of the bitstream at higher bitrates, resulting in greater gains. Furthermore, our approach and PCGCv2 outperform traditional codecs, while PCGC only falls behind V-PCC. This demonstrates promising capability of learning-based approaches for point cloud geometry compression.

C. Ablation Studies

To further validate the effectiveness of our proposed scheme, we provide the bitstream composition, residual features, visualization results, RD performance on point cloud with different geometry precision, and runtime comparisons.

1) *Bitstream composition:* To investigate the cost of geometric priors introduced in our approach, we present the bitstream composition at different bitrate levels, as illustrated in Fig. 7. For each bitrate level, we report the percentage of bits in terms of downsampled coordinates, residual features, and

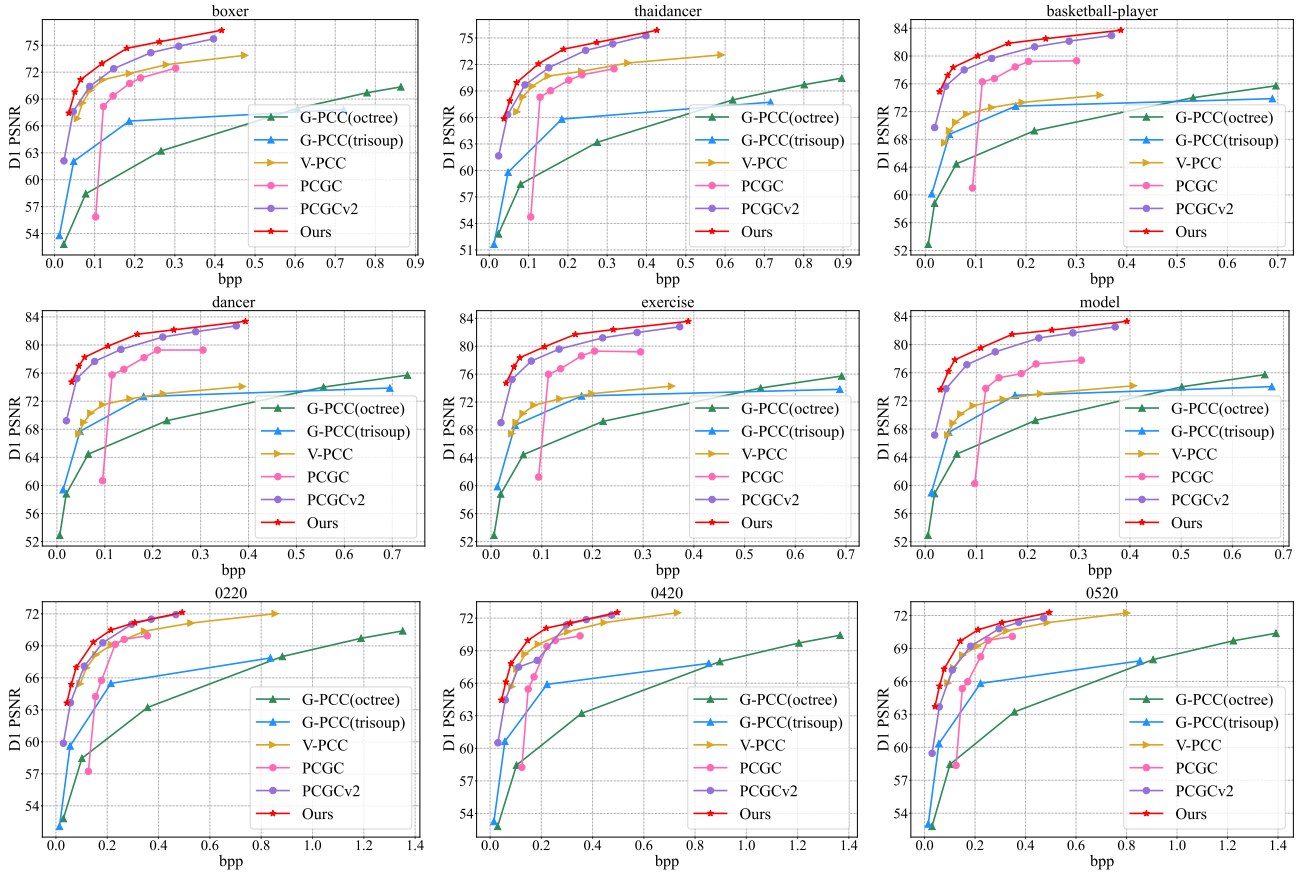


Fig. 6. The RD performance of the proposed approach and baselines on OwlII [67], 8iVSLF [69], and THuman2.0 [68] datasets using D1 error [70], [71].

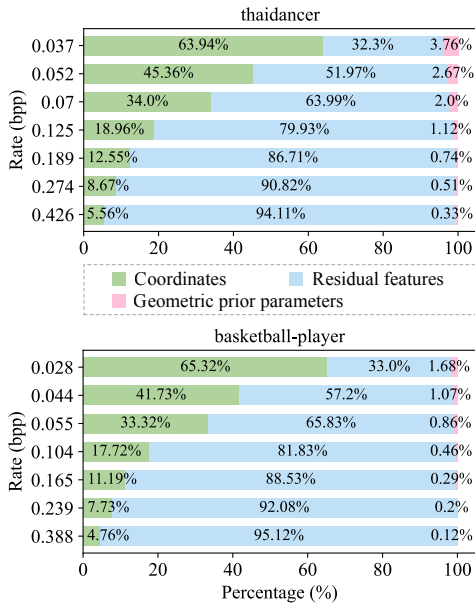


Fig. 7. The bitstream composition at different bitrate levels.

geometric prior parameters. In particular, we can see that geometric parameters account for a small portion of the total bits, with less than 3.8% in the sequence *thaidancer* and at most 1.7% in the sequence *basketball-player*. More importantly, it is observed that the proportion of bits allocated to geometric

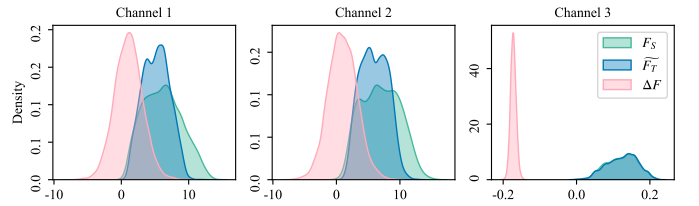


Fig. 8. The distributions of features of the source point cloud F_S , warped features of the aligned point cloud F_T , and residual features ΔF in different channels.

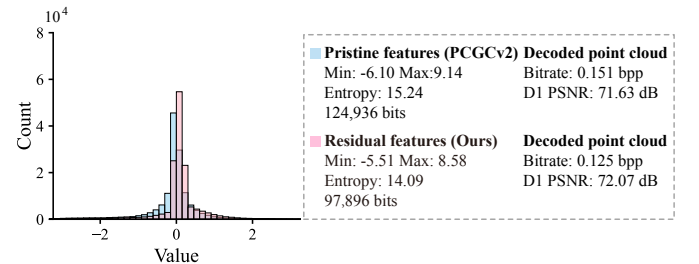


Fig. 9. The histogram, value range, entropy, and corresponding decoded point cloud information of pristine features and residual features.

prior parameters decreases as the bitrate increases. This is because the quantized 86 parameters require approximately 1,368 bits, and residual features become the primary consumer of bits. For higher bitrates, bits of geometric prior parameters

can take up less than 0.5%, while residual features occupy more than 90%. This demonstrates that our method has the potential to reduce the number of bits required for features with negligible cost by utilizing geometric prior parameters.

2) *Analysis of residual features*: Fig. 8 showcases the distribution of two features before and after residual feature computation, as described in Eqn. (6). The residual feature $\Delta\mathbf{F}$ in our framework, represented by the pink area in Fig. 8, has a more concentrated distribution in different channels compared to the feature of the source point cloud \mathbf{F}_S and the warped feature of the aligned point cloud $\tilde{\mathbf{F}}_T$. As the residual features are further encoded by the entropy bottleneck, we compare two cases: compressing pristine features with PCGCv2 and compressing residual features with our approach. From the histogram in Fig. 9, it is apparent that the residual feature has more values near zero and a limited value range. As a result, the entropy of the residual feature is smaller at 14.09 compared to 15.24 for the pristine feature. Furthermore, although the residual feature requires fewer bits at 97,896 compared to 124,936 for the pristine feature, the reconstructed point cloud has better quality with 0.44 dB gain in terms of D1 PSNR. This demonstrates that residual features require fewer bits while maintaining better information fidelity compared to directly compressing pristine features.

3) *Qualitative evaluations*: We visualize the reconstructed point clouds from different point cloud geometry compression methods. Fig. 10 and Fig. 11 display the overall geometry of the whole point cloud, a zoomed-in region with geometry details, and an error map in terms of D1 distance for the sequences *thaidancer* and *0520*, respectively. Compared to other baselines, our proposed approach can generate high-quality decoded point cloud geometry with lower bitrates. In Fig. 10, our method better reconstructs the pleats on the skirt with the least bpp, while the same regions are smoother with PCGCv2 and visible holes are introduced with PCGCv1. Although V-PCC achieves satisfactory reconstruction results in local regions at a higher bitrate, there are apparent cracks in the vertical middle due to the patch generation operations. While G-PCC (octree) leads to a massive loss of points, G-PCC (trisoup) yields comparable visualization results overall but produces cluttered protruding local areas. The visualization of the sequence *0520* also shows similar results in Fig. 11. For instance, our proposed method reconstructs the clear shape of the nose and mouth, while the results from PCGCv2 are smoother with more holes. Additionally, there are obvious distortions on 3D block boundaries from PCGCv1 as it depends on cube partition of a point cloud during inference.

4) *Geometry precision*: To further investigate the effectiveness of the proposed method, we also compare the performance to PCGCv2 using point clouds of the same sequences with different geometry precision levels, as shown in Fig. 12. It can be observed that our proposed scheme demonstrates improved coding performance for both 10-bit and 11-bit point clouds. More specifically, our scheme gains 29.31% bit savings for an 11-bit point cloud *basketball player* and 19.08% for its 10-bit version compared to PCGCv2. This is because higher geometry precision booms the amount of data required to compress point clouds. These results are consistent with those

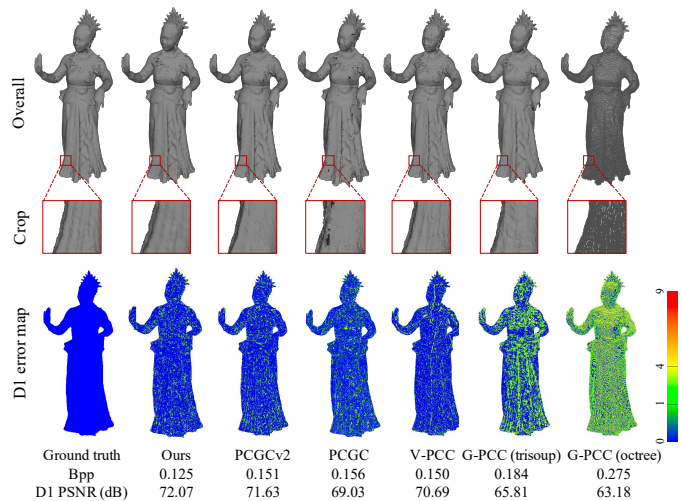


Fig. 10. Visualization of geometry reconstruction results of the sequence *thaidancer* from our method, PCGCv2, PCGC, V-PCC, G-PCC (trisoup), and G-PCC (octree). It is worth mentioning that areas within the red rectangles in the first row are zoomed-in in the second row. The final row exhibits error maps between reconstructed point clouds and ground truth in terms of D1.

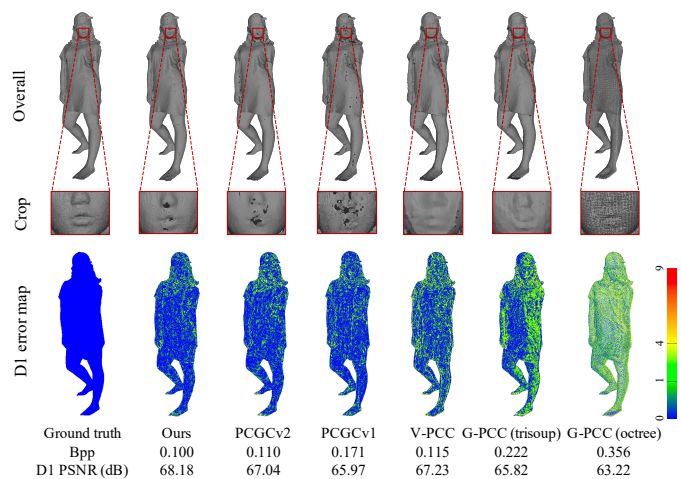


Fig. 11. Visualization of geometry reconstruction results of the sequence *0520*. Areas within the red rectangles in the first row are zoomed-in in the second row. The final row exhibits error maps between reconstructed point clouds and ground truth in terms of D1.

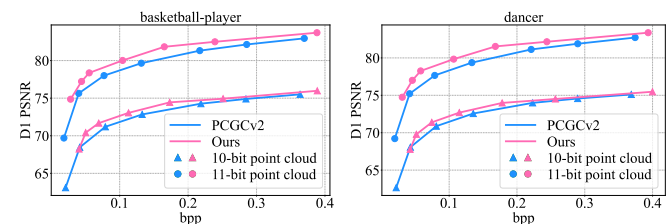


Fig. 12. The RD performance of our method and PCGCv2 on sequences with different geometry precision.

shown in Table II, where BD-Rate gains for the OwlII dataset are much higher than for other datasets. As human point clouds with higher geometry precision allow for larger and finer granularity of 3D coordinates, our method facilitates reconstructing high-accuracy human point clouds.

TABLE III
THE AVERAGE RUNNING TIME (S) IN DIFFERENT APPROACHES

	G-PCC (octree)	G-PCC (trisoup)	V-PCC	PCGCv2	Ours
Enc.	3.147	16.101	82.632	1.500	13.30
Dec.	1.086	13.207	2.094	0.770	2.76

5) *Runtime comparisons*: We further compare the running time of our proposed method and other baseline approaches. We conduct the experiments on a server with an Intel Core i7-10700 CPU and a NVIDIA GeForce RTX 3090 GPU. Following [9], [49], we compute the encoding and decoding time of all testing point clouds at the highest bitrate level since the runtime of G-PCC varies at different bitrate levels. It is worth noting that traditional codecs G-PCC and V-PCC are applied using C++ with a CPU, while learning-based PCGCv2 and our method are implemented using Python with a GPU. As a general indication of computational complexity, Table III shows that our method increases encoding and decoding time compared to PCGCv2. This is because our approach needs to perform additional mesh regression, mesh manipulation, mesh-to-point-cloud conversion, feature extraction, and feature warping in the encoder, and extra mesh manipulation and feature warping are executed in the decoder. The mesh regression and mesh-to-point-cloud conversion methods used are time-consuming, taking around 9.7 s and 1.9 s individually. Our approach can be further sped up with efficient mesh processing algorithms. Furthermore, it is worth mentioning that G-PCC (trisoup) is also based on surface sampling and its encoding time (16.101 s) and decoding time (13.207 s) are higher than our method's encoding time (13.30 s) and decoding time (2.76 s).

V. CONCLUSIONS

In this work, we have proposed a novel deep human point cloud geometry compression scheme based on geometric priors. The novelty of our approach lies in representing human point clouds as a combination of geometric priors and structure variations. By using geometric prior parameters which are quite compact, our method is able to perform feature-level residual operations to remove geometry redundancy. The superior RD performance of the proposed scheme is demonstrated by comparing to traditional and learning-based methods on human point clouds from various datasets. It significantly reduces the rate while preserving the same level in terms of D1 and D2 PSNR. The proposed scheme also achieves the improvement in visual quality with finer geometry details in local areas with the same bitrate.

REFERENCES

[1] E. d'Eon, B. Harrison, T. Myers, and P. A. Chou, "8i voxelized full bodies (a voxelized point cloud dataset)," ISO/IEC JTC1/SC29/WG11, Geneva, Tech. Rep. M40059/M74006, January 2017.

[2] D. Graziosi, O. Nakagami, S. Kuma, A. Zaghetto, T. Suzuki, and A. Tabatabai, "An overview of ongoing point cloud compression standardization activities: Video-based (V-PCC) and geometry-based (G-PCC)," *APSIPA Trans. Signal Inf. Process.*, vol. 9, p. e13, 2020.

[3] S. Schwarz, M. Preda, V. Baroncini, M. Budagavi, P. César, P. A. Chou, R. A. Cohen, M. Krivokuca, S. Lasserre, Z. Li, J. Llach, K. Mammou, R. Mekuria, O. Nakagami, E. Siahaan, A. J. Tabatabai, A. M. Tourapis, and V. Zakharchenko, "Emerging mpeg standards for point cloud compression," *IEEE J. Emerg. Sel. Topics Circuits Syst.*, vol. 9, no. 1, pp. 133–148, 2019.

[4] MPEG 3D Graphics Coding, "V-PCC codec description," ISO/IEC JTC 1/SC 29/WG 7, Tech. Rep. N00100, October 2020.

[5] MPEG 3D Graphics Coding, "G-PCC codec description," ISO/IEC JTC 1/SC 29/WG 7, Tech. Rep. N0099, April 2021.

[6] J. Ballé, V. Laparra, and E. P. Simoncelli, "End-to-end optimized image compression," in *5th Int. Conf. Learn. Representations (ICLR)*, 2017.

[7] J. Ballé, D. Minnen, S. Singh, S. J. Hwang, and N. Johnston, "Variational image compression with a scale hyperprior," in *6th Int. Conf. Learn. Representations (ICLR)*, 2018.

[8] M. Quach, G. Valenzise, and F. Dufaux, "Learning convolutional transforms for lossy point cloud geometry compression," in *IEEE Int. Conf. Image Process. (ICIP)*, 2019, pp. 4320–4324.

[9] J. Wang, D. Ding, Z. Li, and Z. Ma, "Multiscale point cloud geometry compression," in *31st Data Compression Conf. (DCC)*, 2021, pp. 73–82.

[10] J. Wang, D. Ding, Z. Li, X. Feng, C. Cao, and Z. Ma, "Sparse tensor-based multiscale representation for point cloud geometry compression," *IEEE Trans. Pattern Anal. Mach. Intell.*, pp. 1–18, 2022.

[11] R. Mekuria, K. Blom, and P. Cesar, "Design, implementation, and evaluation of a point cloud codec for tele-immersive video," *IEEE Trans. Circuits Syst. Video Technol.*, vol. 27, no. 4, pp. 828–842, 2016.

[12] G. J. Sullivan, J. Ohm, W. Han, and T. Wiegand, "Overview of the high efficiency video coding (HEVC) standard," *IEEE Trans. Circuits Syst. Video Technol.*, vol. 22, no. 12, pp. 1649–1668, 2012.

[13] E. Ramalho, E. Peixoto, and E. Medeiros, "Silhouette 4d with context selection: Lossless geometry compression of dynamic point clouds," *IEEE Signal Process. Lett.*, vol. 28, pp. 1660–1664, 2021.

[14] E. Peixoto, "Intra-frame compression of point cloud geometry using dyadic decomposition," *IEEE Signal Process. Lett.*, vol. 27, pp. 246–250, 2020.

[15] X. Zhang, W. Gao, and S. Liu, "Implicit geometry partition for point cloud compression," in *Data Compression Conf. (DCC)*, 2020, pp. 73–82.

[16] C. Wang, W. Zhu, Y. Xu, Y. Xu, and L. Yang, "Point-voting based point cloud geometry compression," in *23rd Int. Workshop Multimedia Signal Process. (MMSP)*, 2021, pp. 1–5.

[17] A. Ahmmed, M. Paul, M. M. Murshed, and D. Taubman, "Dynamic point cloud geometry compression using cuboid based commonality modeling framework," in *2021 IEEE Int. Conf. Image Process. (ICIP)*, 2021, pp. 2159–2163.

[18] L. Li, Z. Li, S. Liu, and H. Li, "Efficient projected frame padding for video-based point cloud compression," *IEEE Trans. Multimedia*, vol. 23, pp. 2806–2819, 2021.

[19] L. Li, Z. Li, V. Zakharchenko, J. Chen, and H. Li, "Advanced 3d motion prediction for video-based dynamic point cloud compression," *IEEE Trans. Image Process.*, vol. 29, pp. 289–302, 2020.

[20] J. Xiong, H. Gao, M. Wang, H. Li, K. N. Ngan, and W. Lin, "Efficient geometry surface coding in v-pcc," *IEEE Trans. Multimedia*, pp. 1–1, 2022.

[21] P. de Oliveira Rente, C. Brites, J. Ascenso, and F. Pereira, "Graph-based static 3d point clouds geometry coding," *IEEE Trans. Multimedia*, vol. 21, no. 2, pp. 284–299, 2019.

[22] W. Zhu, Y. Xu, D. Ding, Z. Ma, and M. Nilsson, "Lossy point cloud geometry compression via region-wise processing," *IEEE Trans. Circuits Syst. Video Technol.*, vol. 31, no. 12, pp. 4575–4589, 2021.

[23] W. Zhu, Z. Ma, Y. Xu, L. Li, and Z. Li, "View-dependent dynamic point cloud compression," *IEEE Trans. Circuits Syst. Video Technol.*, vol. 31, no. 2, pp. 765–781, 2021.

[24] M. Krivokuca, P. A. Chou, and M. Koroteev, "A volumetric approach to point cloud compression-part II: geometry compression," *IEEE Trans. Image Process.*, vol. 29, pp. 2217–2229, 2020.

[25] R. L. de Queiroz and P. A. Chou, "Motion-compensated compression of dynamic voxelized point clouds," *IEEE Trans. Image Process.*, vol. 26, no. 8, pp. 3886–3895, 2017.

[26] D. C. Garcia, T. A. da Fonseca, R. U. Ferreira, and R. L. de Queiroz, "Geometry coding for dynamic voxelized point clouds using octrees and multiple contexts," *IEEE Trans. Image Process.*, vol. 29, pp. 313–322, 2020.

[27] D. Thanou, P. A. Chou, and P. Frossard, "Graph-based compression of dynamic 3d point cloud sequences," *IEEE Trans. Image Process.*, vol. 25, no. 4, pp. 1765–1778, 2016.

- [28] L. Huang, S. Wang, K. Wong, J. Liu, and R. Urtasun, "Octsqueeze: Octree-structured entropy model for lidar compression," in *IEEE Int. Conf. Comput. Vision Pattern Recognit. (CVPR)*, 2020, pp. 1310–1320.
- [29] Z. Que, G. Lu, and D. Xu, "Voxelcontext-net: An octree based framework for point cloud compression," in *IEEE Int. Conf. Comput. Vision Pattern Recognit. (CVPR)*, 2021, pp. 6042–6051.
- [30] C. Fu, G. Li, R. Song, W. Gao, and S. Liu, "Octattention: Octree-based large-scale contexts model for point cloud compression," in *36th AAAI Conf. Artif. Intell. (AAAI)*, 2022, pp. 625–633.
- [31] T. Fan, L. Gao, Y. Xu, D. Wang, and Z. Li, "Multiscale latent-guided entropy model for lidar point cloud compression," *arXiv:2209.12512*, 2022.
- [32] S. Biswas, J. Liu, K. Wong, S. Wang, and R. Urtasun, "Muscle: Multi sweep compression of lidar using deep entropy models," in *Conf. Neural Inf. Process. Syst. (NeurIPS)*, 2020.
- [33] Z. Hu, G. Lu, and D. Xu, "FVC: A new framework towards deep video compression in feature space," in *IEEE Int. Conf. Comput. Vision Pattern Recognit. (CVPR)*, 2021, pp. 1502–1511.
- [34] G. Lu, W. Ouyang, D. Xu, X. Zhang, C. Cai, and Z. Gao, "DVC: an end-to-end deep video compression framework," in *IEEE Int. Conf. Comput. Vision Pattern Recognit. (CVPR)*, 2019, pp. 11 006–11 015.
- [35] M. Quach, G. Valenzise, and F. Dufaux, "Improved deep point cloud geometry compression," in *22nd Int. Workshop Multimedia Signal Process. (MMSP)*, 2020, pp. 1–6.
- [36] D. T. Nguyen, M. Quach, G. Valenzise, and P. Duhamel, "Learning-based lossless compression of 3d point cloud geometry," in *IEEE Int. Conf. Acoustics Speech Signal Process. (ICASSP)*, 2021, pp. 4220–4224.
- [37] D. T. Nguyen, M. Quach, Giuseppe Valenzise, and P. Duhamel, "Multi-scale deep context modeling for lossless point cloud geometry compression," in *IEEE Int. Conf. Multimedia Expo Workshops (ICMEW)*, 2021, pp. 1–6.
- [38] A. F. R. Guarda, N. M. M. Rodrigues, and F. Pereira, "Deep learning-based point cloud geometry coding with resolution scalability," in *22nd Int. Workshop Multimedia Signal Process. (MMSP)*, 2020, pp. 1–6.
- [39] A. F. R. Guarda, N. M. M. Rodrigues, and F. Pereira, "Point cloud geometry scalable coding with a single end-to-end deep learning model," in *IEEE Int. Conf. Image Process. (ICIP)*, 2020, pp. 3354–3358.
- [40] A. F. R. Guarda, N. M. M. Rodrigues, and F. Pereira, "Point cloud geometry scalable coding with a single end-to-end deep learning model," in *IEEE Int. Conf. Image Process. (ICIP)*, 2020, pp. 3354–3358.
- [41] S. Milani, "ADAE: adversarial distributed source autoencoder for point cloud compression," in *IEEE Int. Conf. Image Process. (ICIP)*, 2021, pp. 3078–3082.
- [42] J. Wang, H. Zhu, H. Liu, and Z. Ma, "Lossy point cloud geometry compression via end-to-end learning," *IEEE Trans. Circuits Syst. Video Technol.*, vol. 31, no. 12, pp. 4909–4923, 2021.
- [43] A. Brock, T. Lim, J. M. Ritchie, and N. Weston, "Generative and discriminative voxel modeling with convolutional neural networks," *arXiv:1608.04236*, 2016.
- [44] R. Xue, J. Wang, and Z. Ma, "Efficient lidar point cloud geometry compression through neighborhood point attention," *arXiv:2208.12573*, 2022.
- [45] Z. Liang and F. Liang, "Transpcc: Towards deep point cloud compression via transformers," in *ICMR '22: International Conference on Multimedia Retrieval, Newark, NJ, USA, June 27 - 30, 2022*, 2022, pp. 1–5.
- [46] Y. He, X. Ren, D. Tang, Y. Zhang, X. Xue, and Y. Fu, "Density-preserving deep point cloud compression," in *IEEE Int. Conf. Comput. Vision Pattern Recognit. (CVPR)*, 2022, pp. 2323–2332.
- [47] M. A. A. Muzaddid and W. J. Beksi, "Variable rate compression for raw 3d point clouds," in *Int. Conf. Robot. Autom. (ICRA)*, 2022, pp. 8748–8755.
- [48] K. You and P. Gao, "Patch-based deep autoencoder for point cloud geometry compression," in *ACM Multimedia Asia*, 2021, pp. 30:1–30:7.
- [49] A. Akhtar, Z. Li, and G. V. der Auwera, "Inter-frame compression for dynamic point cloud geometry coding," *arXiv:2207.12554*, 2022.
- [50] T. Fan, L. Gao, Y. Xu, Z. Li, and D. Wang, "D-DPCC: deep dynamic point cloud compression via 3d motion prediction," in *31st Int. Joint Conf. Artif. Intell. (IJCAI)*, 2022, pp. 898–904.
- [51] W. Yang, Z. Chen, C. Chen, G. Chen, and K. K. Wong, "Deep face video inpainting via UV mapping," *IEEE Trans. Image Process.*, vol. 32, pp. 1145–1157, 2023.
- [52] J. Lin, Y. Yuan, T. Shao, and K. Zhou, "Towards high-fidelity 3d face reconstruction from in-the-wild images using graph convolutional networks," in *IEEE Int. Conf. Comput. Vision Pattern Recognit. (CVPR)*, 2020, pp. 5890–5899.
- [53] F. Wimbauer, S. Wu, and C. Rupprecht, "De-rendering 3d objects in the wild," in *IEEE Int. Conf. Comput. Vision Pattern Recognit. (CVPR)*, 2022, pp. 18 469–18 478.
- [54] S. Wu, C. Rupprecht, and A. Vedaldi, "Unsupervised learning of probably symmetric deformable 3d objects from images in the wild," in *IEEE Int. Conf. Comput. Vision Pattern Recognit. (CVPR)*, 2020, pp. 1–10.
- [55] B. Chen, Z. Wang, B. Li, S. Wang, S. Wang, and Y. Ye, "Interactive face video coding: A generative compression framework," *arXiv:2302.09919*, 2023.
- [56] R. Hanocka, G. Metzger, R. Giryes, and D. Cohen-Or, "Point2mesh: a self-prior for deformable meshes," *ACM Trans. Graph.*, vol. 39, no. 4, p. 126, 2020.
- [57] X. Wei, Z. Chen, Y. Fu, Z. Cui, and Y. Zhang, "Deep hybrid self-prior for full 3d mesh generation," in *IEEE/CVF Int. Conf. Computer Vision (ICCV)*, 2021, pp. 5785–5794.
- [58] D. Smirnov, M. Bessmeltsev, and J. Solomon, "Learning manifold patch-based representations of man-made shapes," in *9th Int. Conf. Learn. Representations (ICLR)*, 2021.
- [59] M. Loper, N. Mahmood, J. Romero, G. Pons-Moll, and M. J. Black, "SMPL: a skinned multi-person linear model," *ACM Trans. Graph.*, vol. 34, no. 6, pp. 248:1–248:16, 2015.
- [60] C. Xu, Y. Makihara, X. Li, and Y. Yagi, "Occlusion-aware human mesh model-based gait recognition," *IEEE Trans. Inf. Forensics Secur.*, vol. 18, pp. 1309–1321, 2023.
- [61] C. R. Qi, L. Yi, H. Su, and L. J. Guibas, "Pointnet++: Deep hierarchical feature learning on point sets in a metric space," in *Conf. Neural Inf. Process. Syst. (NeurIPS)*, 2017, pp. 5099–5108.
- [62] R. Bridson, "Fast poisson disk sampling in arbitrary dimensions," in *ACM SIGGRAPH Sketches*, M. Alexa and A. Finkelstein, Eds., 2007, p. 22.
- [63] B. Graham, M. Engelcke, and L. van der Maaten, "3d semantic segmentation with submanifold sparse convolutional networks," in *IEEE Int. Conf. Comput. Vision Pattern Recognit. (CVPR)*, 2018, pp. 9224–9232.
- [64] C. B. Choy, J. Gwak, and S. Savarese, "4d spatio-temporal convnets: Minkowski convolutional neural networks," in *IEEE Int. Conf. Comput. Vision Pattern Recognit. (CVPR)*, 2019, pp. 3075–3084.
- [65] J. Gwak, C. B. Choy, and S. Savarese, "Generative sparse detection networks for 3d single-shot object detection," in *16th European Conf. Computer Vision (ECCV)*, vol. 12349, 2020, pp. 297–313.
- [66] D. Minnen, J. Ballé, and G. Toderici, "Joint autoregressive and hierarchical priors for learned image compression," in *Conf. Neural Inf. Process. Syst. (NeurIPS)*, 2018, pp. 10 794–10 803.
- [67] Y. Xu, Y. Lu, and Z. Wen, "Owlii dynamic human mesh sequence dataset," ISO/IEC JTC1/SC29 WG11, Macau, Tech. Rep. M41658, October 2017.
- [68] T. Yu, Z. Zheng, K. Guo, P. Liu, Q. Dai, and Y. Liu, "Function4d: Real-time human volumetric capture from very sparse consumer RGBD sensors," in *IEEE Int. Conf. Comput. Vision Pattern Recognit. (CVPR)*, 2021, pp. 5746–5756.
- [69] M. Krivokuća, P. A. Chou, and P. Savill, "8i voxelized surface light field (8iVSLF) dataset," ISO/IEC JTC1/SC29 WG11, Ljubljana, Tech. Rep. M42914, July 2018.
- [70] 3DG, "Common test conditions for V3C and V-PCC," ISO/IEC JTC 1/SC 29/WG 11, Tech. Rep. N19518, July 2020.
- [71] 3DG, "Common test conditions for G-PCC," ISO/IEC JTC 1/SC 29/WG 11, Tech. Rep. N19584, July 2020.